

Quantifying surface losses in superconducting aluminum microwave resonators

Elizabeth Hedrick,¹ Faranak Bahrami,¹ Alexander C. Pakpour-Tabrizi,¹ Atharv Joshi,¹ Q. Rumman Rahman,¹ Ambrose Yang,¹ Ray D. Chang,¹ Matthew P. Bland,¹ Apoorv Jindal,¹ Guangming Cheng,² Nan Yao,² Robert J. Cava,³ Andrew A. Houck,¹ and Nathalie P. de Leon¹

¹*Department of Electrical and Computer Engineering, Princeton University, Princeton, New Jersey 08540, USA*

²*Princeton Materials Institute, Princeton University, Princeton, New Jersey 08540, USA*

³*Department of Chemistry, Princeton University, Princeton, New Jersey 08540, USA*

The recent realization of millisecond-scale coherence with tantalum-on-silicon transmon qubits showed that depositing the Al/AlO_x/Al Josephson junction in a high purity, ultrahigh vacuum environment was critical for achieving lifetime-limited coherence [1], motivating careful examination of the aluminum surface two-level system (TLS) bath. Here, we measure the microwave absorption arising from surface TLSs in superconducting aluminum resonators, following methodology developed for tantalum resonators [2]. We vary film and surface properties and correlate microwave measurements with materials characterization. We find that the lifetimes of superconducting aluminum resonators are primarily limited by surface losses associated with TLSs in the 2.7 nm-thick native AlO_x. Treatment with 49% HF removes surface AlO_x completely; however, rapid oxide regrowth limits improvements in surface loss and long term device stability. Using these measurements we estimate that TLSs in aluminum interfaces contribute around 27% of the relaxation rate of state-of-the-art tantalum-on-silicon qubits that incorporate aluminum-based Josephson junctions.

I. INTRODUCTION

Superconducting circuits are a leading platform for the realization of quantum processors and have achieved several landmark demonstrations, including beyond-threshold quantum error correction [3–8], long-lived quantum memories [9–11], and quantum simulation [12–15]. Despite substantial progress, state-of-the-art superconducting qubits continue to suffer from dielectric loss arising from amorphous materials, impurities, and defects [2, 16–20]. Recent advances in materials engineering have enabled millisecond-scale lifetimes (T_1) and coherence times (T_2) by utilizing tantalum and high purity silicon [1], driven by precise quantification of the different contributions to loss and addressing the TLS-related loss associated with surface contamination, surface oxides, and the bulk substrate [1, 2, 21–23]. These millisecond-scale tantalum qubits still incorporate the traditional aluminum / aluminum oxide material stack for the Josephson junction. Therefore, a natural next step is to directly quantify the TLS losses in the native aluminum oxide to determine their contributions to the performance of state-of-the-art qubits.

The Josephson junction contains amorphous oxides both on the exposed surfaces of the junction and within the junction tunneling barrier that are known to host two-level systems (TLSs) [24–28], which give rise to dielectric losses and qubit dephasing. Fabricating Josephson junctions in an ultrahigh vacuum (UHV) ($<10^{-9}$ mbar background pressure) environment with a low background pressure of O₂, H₂O, and hydrocarbons has already enabled the realization of transmons with lifetime-limited coherence times, demonstrating that the TLS losses associated with Josephson junction fabrication can be mitigated by improved processing and materials optimization [1]. In order to study these oxides and evaluate mitigation strategies, we study the power and temperature dependence of losses in aluminum superconducting resonators to quantify the contributions of different sources of loss. We vary fabrication and post-fabrication techniques aimed at decreasing the TLS bath on the surfaces of aluminum coplanar waveguide (CPW) resonators and extract the quality factor limit imposed by linear

absorption associated with TLS ($Q_{\text{TLS},0}$) [2]. We then correlate the chemical, structural, and morphological properties of aluminum resonators with their microwave behavior (Fig. 1).

We focus on variations associated with thin film properties, fabrication methods, and post-fabrication processes. We find that aluminum resonators have over three times higher surface dielectric losses than state-of-the-art tantalum resonators. We evaluate the chemical compatibility of various post-fabrication processing steps with aluminum. These losses can be partially offset by device treatment in hydrofluoric (HF) acid, which decreases the losses by a factor of 1.8, approximately matching the performance of tantalum resonators with their native surface oxide and no oxide stripping process [2]. However, the growth rate of the native oxide of aluminum is faster than that of tantalum, giving a shorter time window in ambient conditions before the full native oxide thickness has regrown. Based on our studies we estimate that the aluminum oxides associated with the Josephson junction account for 27% of the relaxation rate of state-of-the-art tantalum-on-silicon qubits.

II. RESULTS

We first investigate the structural and dc transport properties of aluminum films grown under different deposition conditions. We tune the deposition rate (0.2 - 0.4 nm/s) and temperature (-72 °C to 200 °C), and vary the growth method (e-beam evaporation or sputtering) and substrate (sapphire or Si), (Materials and Methods). Structural characterization via X-ray diffraction (XRD) and transmission electron microscopy (TEM) diffraction (Online Resource S1 and S2) predominantly show an out-of-plane $\langle 111 \rangle$ orientation for all deposition conditions. However, the relative intensities of the Al ($\langle 111 \rangle$) peak at 38.5° and the sapphire ($\langle 0001 \rangle$) peak at 41.7° vary as we change the deposition temperature (Fig. 2a). The Al film deposited at 200 °C exhibits the highest relative intensity for the $\langle 111 \rangle$ peak, suggesting a greater degree of crystalline orientation with the substrate. The relative peak intensity is reduced by ~25% and ~85% for films deposited at 25 °C and

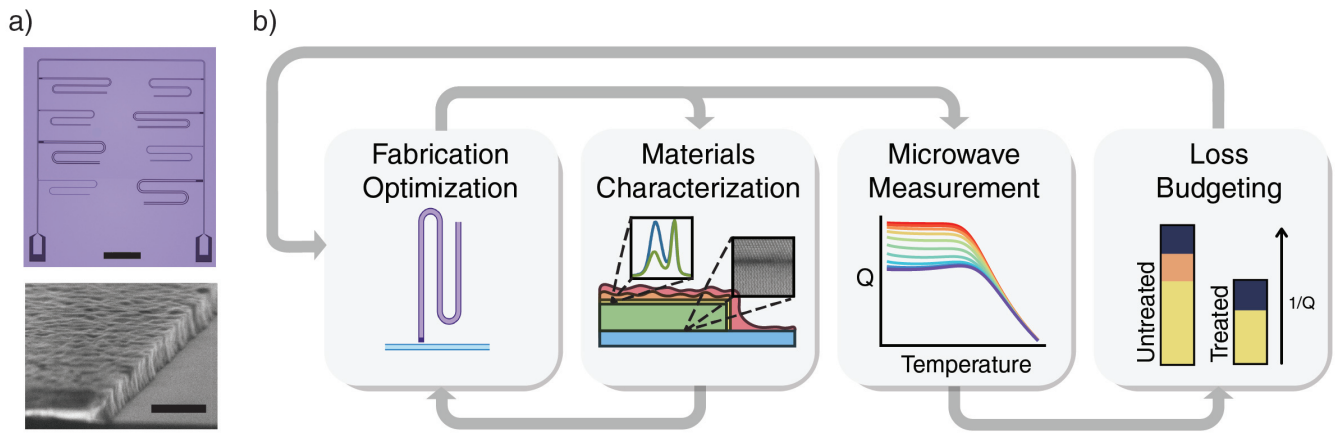


FIG. 1. **Diagnosing sources of loss in superconducting resonators.** a) Top: Optical image of chip containing eight $\lambda/4$ CPW resonators ranging from 2 to 16 μm in pitch capacitively coupled to a microstrip feedline. Scale bar is 500 μm . Bottom: Scanning electron microscope image showing sidewall profile of 200 nm Al deposited on c-plane sapphire deposited at 25°C and fabricated using wet etch. The sidewall is vertical and the film has a lumpy texture. Scale bar is 400 nm. b) Pipeline for measuring materials-related losses using iterative resonator measurement and materials characterization feedback. Microwave measurements provide loss tangents associated with different loss mechanisms, while structural and chemical composition characterization provides candidates for sources of loss. Combined, these measurements allow for estimation of the quantitative contribution of each surface and contaminant to the loss. The cartoon cross section of the superconducting resonator (top) consists of substrate (blue), metal (green), a thin native oxide (yellow), photoresist contamination residue after fabrication (orange), and adventitious hydrocarbons from the atmosphere (red). The metal-substrate (MS) interface and substrate-air (SA) interfaces are represented by a continuous black line. These colors extend to those in the bar graph in the loss budgeting panel.

-72 °C, respectively. We examine the grain texture of these films with AFM (Fig. 2b-d), and we observe that the root-mean-square roughness, S_q , varies by a factor of ~ 10 across the three films. Grain sizes are measured with cross-sectional scanning transmission electron microscopy (STEM) and are found to be larger by a factor of ~ 6.5 for films with a deposition temperature of 200 °C compared to films grown at -72 °C and 25 °C (Table I, Online Resource S1).

We also examine the impact of different growth conditions on the heteroepitaxial metal-substrate (MS) interface. STEM images at the MS interface suggest that both Al films grown on sapphire at 200 °C (Fig. 2f) and on Si at 25 °C (Fig. 2g) feature coherent heteroepitaxy. The Al-substrate interface for films deposited at -72 °C exhibits blurred contrast observed in the STEM image (Fig. 2e), indicating reduced heteroepitaxial quality that propagates into the bulk of the Al film. Combining these observations with the observation that the grain sizes for films deposited at -72 °C and 25 °C are comparable suggests that the lower intensity peak observed in XRD for the films deposited at -72 °C arises from a larger out-of-plane $\langle 111 \rangle$ misalignment (Fig. 2a and e). We do not observe any hydrocarbon contamination at the MS interface with energy-dispersive X-ray spectroscopy (EDS) for any film deposition condition, nor do we see evidence of oxygen contamination at grain boundaries across Al films with varying grain sizes (see Online Resource S1).

We next measure the dc resistivity as a function of temperature for each deposition condition to extract the superconducting transition temperature (T_c) and the residual resistivity ratio (RRR), the ratio of the resistivity at room temperature ($T = 300$ K) to the resistivity right before T_c ($T = 2$ K) (Fig. 2h). The highest observed RRR is in films deposited at 200 °C, $\text{RRR} = 32 \pm 19$, which is larger by a factor of 3 and 6.6 com-

pared to films deposited at -72 °C and 25 °C, respectively. This variation in RRR correlates with film morphology, where the highest RRR values are observed for films that have the largest grain sizes. The superconducting transition temperatures are close to the bulk T_c of 1.2 K [29], ranging from 1.05 K to 1.41 K, and are inversely correlated with grain size.

Film Growth	Roughness (S_q)	Grain size	T_c (K)	RRR
200°C	1.19 nm	87.34 nm	1.05 ± 0.05	32 ± 19
25°C	0.5 nm	12.58 nm	1.41 ± 0.05	4.82 ± 0.007
-72°C	5.11 nm	15.63 nm	1.15 ± 0.05	10.41 ± 0.7

TABLE I. Aluminum thin film surface roughness, average grain size, T_c and residual resistivity ratio (RRR) for films grown at 200°C, 25°C, and -72°C.

We fabricate 40 microwave resonators across nine chips from Al films with different growth conditions (Materials and Methods). We use three different fabrication methods: a lift-off method, in which the aluminum is deposited on top of a patterned resist; a wet-etch method, in which the metal is deposited on the substrate and then the patterned resist serves as an etch mask for etching the device in acid; and a dry-etch method, in which the patterned resist serves as an etch mask for reactive ion etching with chlorine chemistry. We note differences in sidewall morphology dependent on etch method (Online Resource S3). All devices are cleaned by iterative solvent processing to remove residual hydrocarbons without damaging the underlying Al (Materials and Methods).

We measure the internal quality factor, Q_{int} , as a function of temperature and microwave power to disentangle the different microwave loss contributions in Al devices (Fig. 3a) (Online Resource S4). We model Q_{int} with three separate contribu-

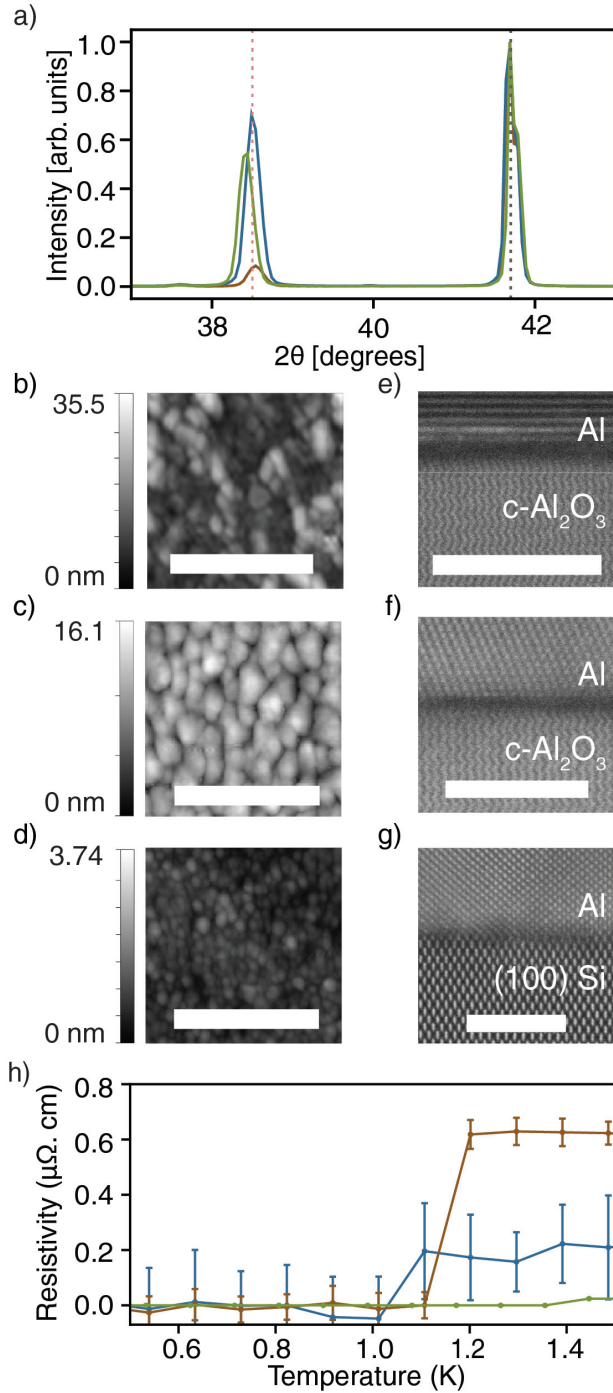


FIG. 2. Aluminum film characterization. a) XRD patterns of three aluminum thin films on $c\text{-Al}_2\text{O}_3$ deposited at -72°C (brown), 25°C (green) and 200°C (blue). Dotted lines show $\text{Al} \langle 111 \rangle$ ($2\theta = 38.5^\circ$) and $c\text{-Al}_2\text{O}_3 \langle 0006 \rangle$ ($2\theta = 41.7^\circ$) crystal directions. b) AFM of 200 nm Al film on $c\text{-Al}_2\text{O}_3$ deposited at -72°C with $S_q = 5.11$ nm and average grain size of 15.63 nm. c) AFM of 200 nm Al film on $c\text{-Al}_2\text{O}_3$ deposited at 200°C with $S_q = 1.19$ nm and average grain size of 87.34 nm. d) AFM of 200 nm Al film on $\langle 100 \rangle$ Si deposited at 25°C with $S_q = 0.5$ nm and average grain size of 12.58 nm. e) TEM of the interface of Al 200 nm film deposited at -72°C with $c\text{-Al}_2\text{O}_3$. Scale bar is 5 nm. f) TEM of the interface of Al 200 nm film deposited at 200°C with $c\text{-Al}_2\text{O}_3$. Scale bar is 5 nm. g) TEM of the interface of Al 200 nm film deposited at room temperature with $\langle 100 \rangle$ Si. Scale bar is 5 nm. h) Resistivity as a function of temperature for films deposited at -72°C (brown), 25°C (green) and 200°C (blue).

tions: Q_{TLS} , the temperature- and power-dependent quality factor due to TLSs; Q_{QP} , the temperature-dependent quality factor due to thermal quasiparticles; and Q_{other} , a power- and temperature-independent term arising from other loss mechanisms (Fig. 3a) [2]. Similar to tantalum devices in the millikelvin temperature and single-photon power regime [2], we observe that at least 84% of total loss in our Al devices is from TLSs. We therefore focus on a fitting parameter that estimates the inverse linear absorption due to TLSs, $Q_{\text{TLS},0}$. We vary the geometry of the device to examine the dependence of $Q_{\text{TLS},0}$ on the surface participation ratio (SPR) of the electromagnetic energy density. We find that $Q_{\text{TLS},0}$ increases as the metal-substrate SPR (p_{MS}) decreases with a linear dependence, indicating that the TLS losses are present in a thin layer at a surface or interface (Fig. 3b, see Online Resource S5). This linear dependence can be interpreted as a dielectric loss tangent ($\tan \delta$) associated with a thin surface or interface dielectric layer of uniform thickness, with contributions from the amorphous surface oxide, hydrocarbon contamination, and defects at the metal–air (MA), MS, and substrate–air (SA) interfaces.

We study the variation of this surface loss tangent with differing fabrication methods (Fig. 3b, Table II). The surface loss tangents associated with wet-etch and lift-off fabrication methods are statistically indistinguishable (within 2σ), and combining the data from both fabrication methods yields a surface loss tangent $\tan \delta = (3.19 \pm 0.22) \times 10^{-3}$, while the dry-etch method yields a surface loss tangent of $\tan \delta = (5.43 \pm 0.14) \times 10^{-3}$ (Fig. 3b, brown data), corresponding to a $\sim 70\%$ increase in TLS loss. Overall our measurements suggest that resonators fabricated from films deposited at 200°C with the wet etch fabrication method result in the best observed device performance; therefore, we use this fabrication procedure for studying the impact of post-fabrication surface treatments.

We use two different post-fabrication surface treatments to mitigate surface losses: a 49% HF acid treatment, and a hydrogen peroxide (H_2O_2) treatment. We evaluate the two post-fabrication surface treatments on the amorphous aluminum oxide and fabrication hydrocarbon residue by comparing the variation in Al2p, O1s, and C1s peaks in X-ray photoelectron spectroscopy (XPS) (Online Resource S6). The Al2p spectrum consists of a pair of peaks split by spin-orbit coupling associated with metallic Al at ~ 72.6 eV and another pair of peaks associated with aluminum oxide at ~ 75 eV. We model the Al2p peaks with two Lorentzian lineshapes for the metallic peaks (Al^0) and Gaussian lineshapes for the non-zero oxidation states (Al_{int} , Al^{3+}) (Fig. 4a). We estimate the oxide thickness from the integrated oxide peak intensity as a function of time in atmosphere over 25 days, and we observe oxidation kinetics characterized by two distinct regimes: a linear regime from 0 - 2.3 nm over the course of 24 hours, followed by a logarithmic dependence thereafter which saturates at around 3 nm, consistent with the Cabrera-Mott model (Fig. 4b) [30–35].

We use 49% HF acid treatment to reduce the amorphous aluminum oxide layer and eliminate hydrocarbon contamination arising from photoresist residue. Comparing a film that has been treated with 49% HF to a reference sample that has been freshly deposited with the same duration of ambient exposure, the aluminum oxide thickness and surface carbon contamination are similar as measured by XPS, indicating that this surface treatment completely removes aluminum surface oxide

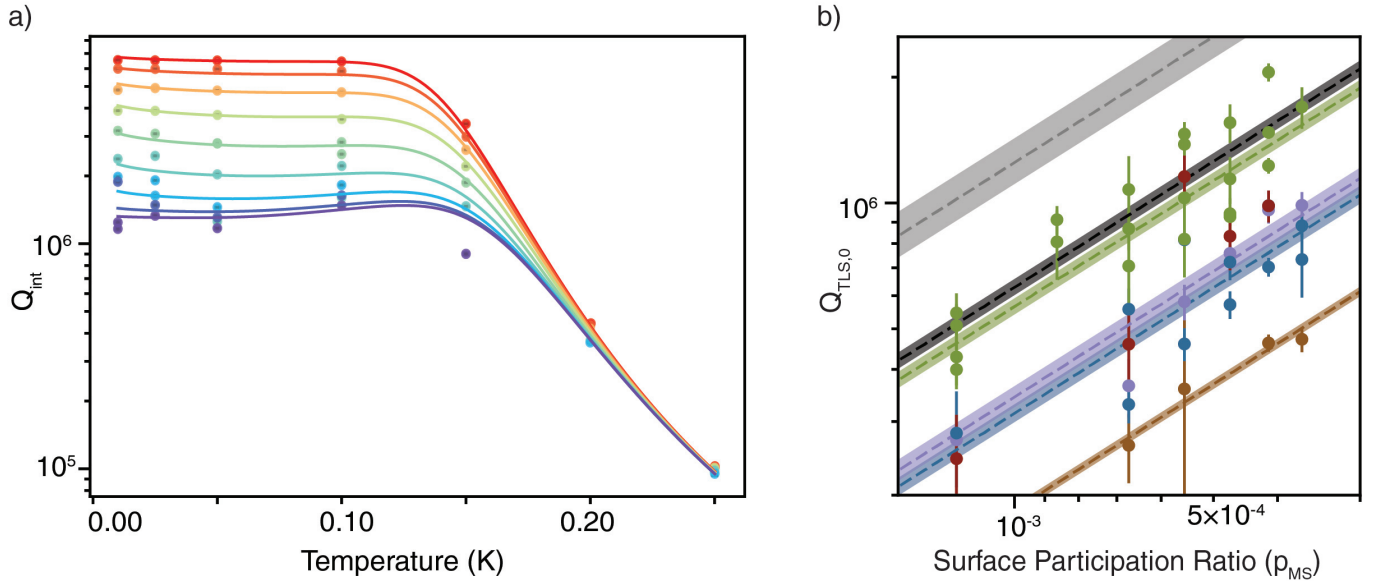


FIG. 3. **Aluminum resonator microwave characterization.** a) Power and temperature dependence of 10 μm pitch CPW resonator. High power (-10 dB, red) decreases by 10 dB until the lowest power (-90 dB, purple). Three regimes are seen: $1/T$ dependence until 25 mK, TLS saturation and increase until 125 mK, and quasiparticle rolloff at 150 mK. Scale bar is 500 μm . b) $Q_{\text{TLS},0}$ as a function of surface participation ratio. Surface loss tangents are fitted according to surface treatment (tantalum surface loss tangents have been added from Ref. [2]); shaded region indicates one standard deviation on fit parameters. From the top, fitted loss tangents are : Ta treated with buffered oxide etch (gray), Ta treated with piranha solution (black), HF-treated Al on sapphire or silicon (green), H_2O_2 -treated Al on sapphire (purple), solvent-treated Al on sapphire (blue), and solvent-treated dry etch Al on sapphire, chlorine chemistry (brown). Red points represent HF-treated resonators remeasured after 3 months of oxide and hydrocarbon saturation.

Chip	Film Deposition	Fabrication method	Surface treatment	Loss Tangent ($\times 10^{-3}$)	Oxide Thickness
Wet etch	200°C, c- Al_2O_3	Wet Etch	untreated	2.53 ± 0.14	2.69 ± 0.07 nm
H_2O_2	200°C, c- Al_2O_3	Wet Etch	H_2O_2	2.91 ± 0.17	2.66 ± 0.07 nm
Cryo	-72°C, c- Al_2O_3	Lift-off	untreated	3.60 ± 0.21	2.73 ± 0.08 nm
Dry etch	200°C, c- Al_2O_3	Reactive Ion Etch	untreated	5.43 ± 0.14	2.70 (est.) nm
H_2O_2 , 49% HF 5s	200°C, c- Al_2O_3	Wet Etch	49% HF	1.86 ± 0.18	1.90 ± 0.05 nm
49% HF, 3 months	200°C, c- Al_2O_3	Wet Etch	HF, oxide saturation	2.51 ± 0.29	3.11 ± 0.09 nm
49% HF 15s	200°C, c- Al_2O_3	Wet Etch	49% HF	1.68 ± 0.14	1.91 ± 0.05 nm
RT, Si, 49% HF 10s	25°C, 100 Si	Wet Etch	49% HF	1.34 ± 0.07	1.87 ± 0.05 nm
RT, Si, 49% HF 10s	25°C, 100 Si	Wet Etch	49% HF	1.95 ± 0.08	2.00 (est.) nm

TABLE II. Individual resonator chip fabrication methods, growth parameters, surface treatments, loss tangents and oxide thicknesses for all devices. Devices listed with estimated (est.) oxide thicknesses are found using the time exposed to air before cryogenic measurement and the corresponding oxide thickness in Fig. 4a.

until re-exposure to air (Fig. 4c, d and e). We minimize the device exposure to atmosphere before cooldown; the device is exposed to ambient conditions for 2-4 hours resulting in a 1.7-2.1 nm aluminum oxide layer thickness (Fig. 4a). The surface loss tangent for the devices with 49% HF acid treatment shows a statistically significant ($>3\sigma$) improvement compared to untreated devices; $\tan \delta = (1.77 \pm 0.08) \times 10^{-3}$ (Fig. 3b, green data), corresponding to a $\sim 40\%$ decrease in surface loss (Table II).

Hydrogen peroxide (H_2O_2) treatment decreases the intensity of the surface hydrocarbon content as measured by the C1s spectrum, while the aluminum oxide thickness and binding energy of the O1s peak remain unaffected (Fig. 4d, e, f). This post-fabrication treatment reduces the surface hydrocarbons in-

cluding fabrication and adventitious hydrocarbon residues by $(34.7 \pm 5.8)\%$; however, we observe no statistically significant improvement, ($<1\sigma$), compared to the surface loss tangent associated with the wet-etch and lift-off fabrication methods with no post-fabrication treatment. Although we observe $\sim 34.7\%$ reduction in the carbon signal on the top surface of the Al device in XPS, we cannot directly assess the differential effectiveness of this treatment on different types of hydrocarbon contamination, namely fabrication residue and adventitious carbon from the atmosphere, using XPS alone. Since the surface losses are unchanged, we conclude that H_2O_2 treatment removes adventitious carbon, but not fabrication residue, and that the latter has a larger contribution to surface loss.

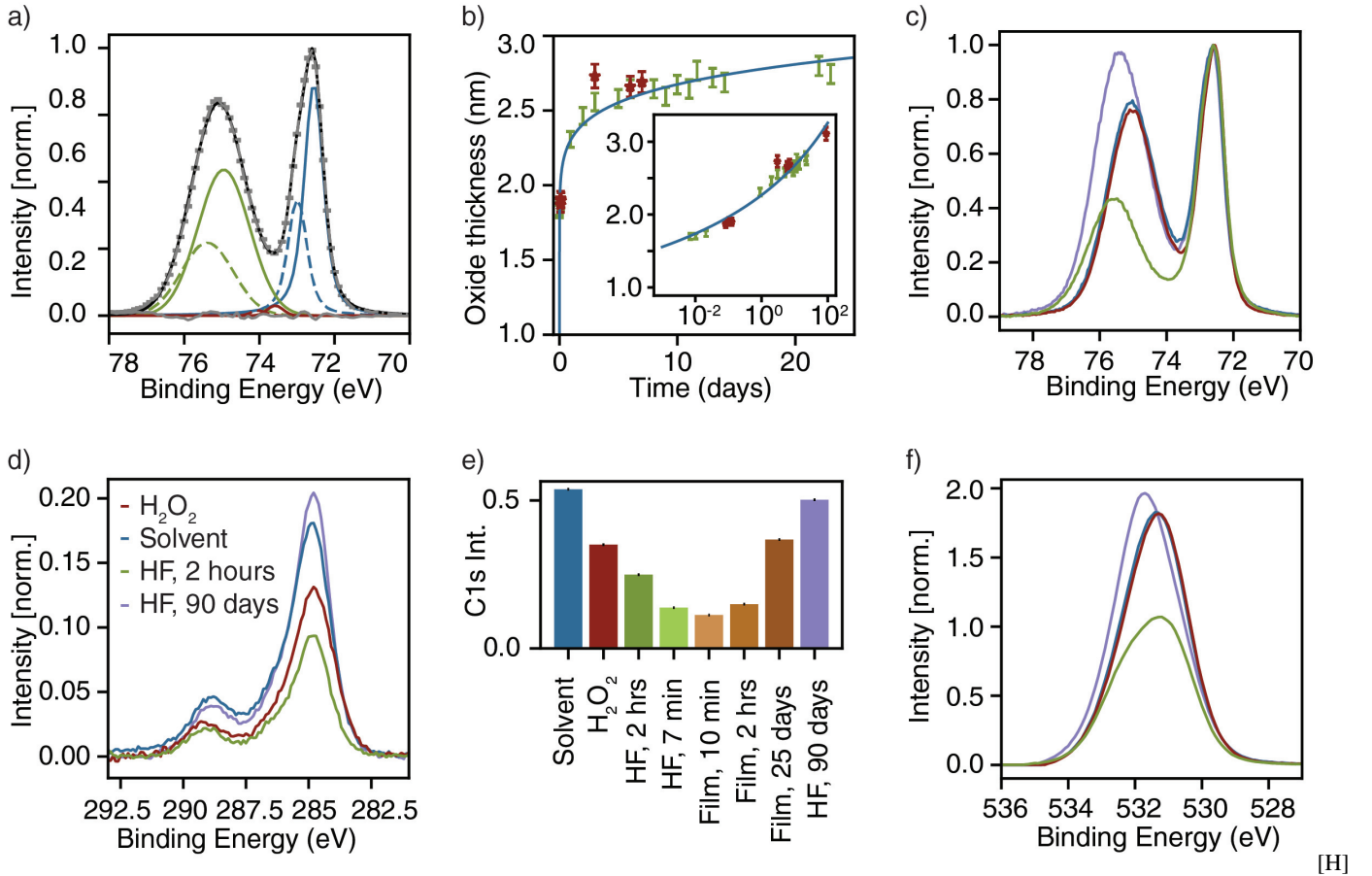


FIG. 4. **Aluminum surface characterization using X-ray Photoelectron Spectroscopy.** a) Example fit of Al₂p peak for a film with 2.69 ± 0.07 nm of native oxide. Each oxidation state (0, 3+, interface) has a 1/2 (dotted) and 3/2 (solid) spin orbital contribution. Using the intensity of oxide peaks to the metal peak, we calculate the oxide thickness using the Strohmeier equation (Online Resource S6). Plot is normalized to intensity. b) Oxide thicknesses calculated for a native oxide on aluminum film (green) as a function of time. The fitted line (blue) shows a linear regime with rapid oxide growth kinetics for roughly the first 12 hours, then an intermediate regime until 24 hours after exposure to air with slower, but still relatively fast growth, followed by a logarithmic dependence which slowly saturates the oxide. Points in red show oxide thicknesses measured from devices. Inset: The same data plotted on semilog axes. c) Al₂p XPS intensity as a function of binding energy. H₂O₂ and solvent-cleaned devices show 2.66 ± 0.07 and 2.69 ± 0.07 nm of oxide growth, respectively, while the HF-cleaned device shows 1.87 ± 0.05 nm of growth. Plots are normalized to intensity, and then scaled so the Al₂p peak height is set to 1 to more easily see differences in oxide thickness. All spectra are shifted to the Al_{3/2}⁰ = 72.6 eV. d) C1s XPS intensity as a function of binding energy normalized to the corresponding intensity of the Al₂p peak. The solvent-cleaned device shows a greater intensity than H₂O₂, which shows a greater intensity than the HF-cleaned device. e) Numerical comparisons of the integral intensities of the C1s peak across devices and films at each of the growth regimes. f) O1s XPS intensity as a function of binding energy normalized to the corresponding intensity of the Al₂p peak. The HF-treatment produces a double peaked structure with a small increase in binding energy, signifying a slight decrease in interfacial oxide between the metallic and 3+ aluminum states. We normalize the peak positions for both Al₂p and O1s to the C1s peak at 284.8 eV and peak intensities for both C1s (Fig. 4d) and O1s (Fig. 4f) to the corresponding Al₂p intensity to accurately compare carbon contamination between different post-fabrication cleaning treatments. [H]

III. DISCUSSION

The comparison between devices without post-fabrication processing and with 49% HF acid treatment suggests that the dominant source of TLS loss in Al devices is the amorphous aluminum oxide at the MA interface. The surface loss tangent for devices without any post-fabrication treatment contains loss contributions from the MA (which includes amorphous aluminum oxide, $\tan \delta_{\text{AlO}_x}$) and hydrocarbon contamination ($\tan \delta_{\text{HC}}$), SA ($\tan \delta_{\text{SA}}$), and MS ($\tan \delta_{\text{MS}}$) interfaces. On the other hand, for the 49% HF acid-treated devices we signif-

icantly reduce the amorphous surface oxide and hydrocarbon contamination by $\sim 29.6\%$ and $\sim 53.6\%$, respectively, and expect the remaining hydrocarbons to be adventitious rather than fabrication residue. We therefore model the total surface loss tangent for these devices with respect to each interface SPR (p_i) and estimated dielectric layer thickness (t_i) normalized to the assumed thickness ($t_0 = 3$ nm) in our SPR simulation as follows (Online Resource S7):

$$\tan \delta_{\text{Al, HF}} = \frac{p_{\text{MA}}}{p_{\text{MS}}} \cdot \frac{t_{\text{HF, AlO}_x}}{t_0} \cdot \tan \delta_{\text{AlO}_x} \quad (1)$$

$$+ \frac{p_{\text{SA}}}{p_{\text{MS}}} \cdot \frac{t_{\text{SA}}}{t_0} \cdot \tan \delta_{\text{SA}} + \frac{t_{\text{MS}}}{t_0} \tan \delta_{\text{MS}}$$

$$\tan \delta_{\text{Al, HF90days}} = \frac{p_{\text{MA}}}{p_{\text{MS}}} \cdot \frac{t_{\text{HF90days, AlO}_x}}{t_0} \cdot \tan \delta_{\text{AlO}_x} \quad (2)$$

$$+ \frac{p_{\text{SA}}}{p_{\text{MS}}} \cdot \frac{t_{\text{SA}}}{t_0} \cdot \tan \delta_{\text{SA}} + \frac{t_{\text{MS}}}{t_0} \tan \delta_{\text{MS}}$$

$$\tan \delta_{\text{Al, untreated}} = \frac{p_{\text{MA}}}{p_{\text{MS}}} \cdot \frac{t_{\text{untreated, AlO}_x}}{t_0} \cdot \tan \delta_{\text{AlO}_x} \quad (3)$$

$$+ \frac{p_{\text{MA}} + p_{\text{SA}}}{p_{\text{MS}}} \cdot \frac{t_{\text{i, HC}}}{t_0} \tan \delta_{\text{HC}}$$

$$+ \frac{p_{\text{SA}}}{p_{\text{MS}}} \cdot \frac{t_{\text{SA}}}{t_0} \cdot \tan \delta_{\text{SA}} + \frac{t_{\text{MS}}}{t_0} \tan \delta_{\text{MS}}$$

We isolate the loss contribution from amorphous aluminum oxide, $\tan \delta_{\text{AlO}_x}$, by comparing the extracted surface loss tangents and the surface oxide thickness for the 49% HF treated aluminum after atmospheric exposure for 2 hours to the same film treatment after exposure for 90 days (Fig. 4c and d, purple data points). We confirm that the oxide thickness and adventitious hydrocarbon signal have saturated after this 90 day period via XPS analysis (see Online Resource S7). We are confident that the MS and SA interfaces of these devices are the same, as they are deposited and fabricated using the same process; therefore, the difference between their loss tangents can be entirely attributed to the change in oxide thicknesses, equal to 1.2 nm.

We therefore estimate the intrinsic material loss tangent of amorphous AlO_x to be $\tan \delta_{\text{AlO}_x} = (1.74 \pm 0.7) \times 10^{-2}$, which can be scaled by surface participation ratios $(p_{\text{MA}}/p_{\text{MS}}) \tan \delta_{\text{AlO}_x} = (1.82 \pm 0.74) \times 10^{-3}$. This value is over three times larger than what is estimated for TaO_x , $\tan \delta_{\text{AlO}_x} = (5 \pm 1) \times 10^{-3}$ ($(p_{\text{MA}}/p_{\text{MS}}) \tan \delta_{\text{TaO}_x} = (6 \pm 1) \times 10^{-4}$) [2].

Using Eq. 1, we can insert $\tan \delta_{\text{AlO}_x}$ to find that the combined, surface-scaled contribution from the SA and MS interfaces is $(6.19 \pm 4.96) \times 10^{-4}$. This is $\sim 50\%$ higher than the TLS loss from the same interfaces in tantalum on sapphire devices [2].

We evaluate the loss contribution from the SA interface to the total surface loss by comparing the resonators measured on sapphire and Si substrates. Sapphire is a chemically inert single crystal, whereas Si can regrow an amorphous surface oxide layer after exposure to air. The 49% HF acid-treated devices are fabricated on both sapphire and Si substrates (Fig. 3b, green data points). The 49% HF acid treatment removes the amorphous silicon oxide layer, leaving a ~ 0.4 nm thick SiO_x layer on the SA interface of the Si devices (Online Resource S7). The surface loss tangent for Al-on-Si devices, however, is within 1σ of their sapphire counterpart devices, suggesting SiO_x has less than 5% contribution to the total surface loss, similar to what has been reported for Ta devices [1].

We next examine the MS interface contribution to the total surface loss by comparing the devices fabricated with the liftoff method (film deposited at -72°C) to the wet-etch method (film deposited at 200°C). While the heteroepitaxial interfaces differ greatly in imaging and structural analysis, the extracted

surface loss tangents display comparable behavior to one another (within 1σ). Similarly, devices with the 49% HF acid treatment on sapphire (film deposited at 200°C) and Si (film deposited at 25°C) also exhibit similar losses. This observation confirms the variations in crystalline orientation, morphology, and heteroepitaxy quality at the MS interface have a negligible contribution to the surface loss for Al resonators.

We observe a peak in the C1s spectrum at 284.8 eV for all devices, with the largest intensity corresponding to untreated devices (Fig. 4d, untreated). This signal includes fabrication residue from photoresist, as well as adventitious carbon from atmospheric exposure. The 49% HF acid treatment strips away the surface oxide and therefore completely eliminates the fabrication contamination residue. We interpret the remaining C1s signal as related to atmospheric adventitious carbon (Fig. 4d, HF, 2 hours). Using the estimated loss tangent for AlO_x in Eq. 1, and assuming that the photoresist residue resides on the MA and SA surfaces, we estimate a loss tangent from photoresist residue to be $\tan \delta_{\text{HC}} = (3.9 \pm 1.1) \times 10^{-3}$ ($(p_{\text{MA}} + p_{\text{SA}})/p_{\text{MS}} \times \tan \delta_{\text{HC}} = (4.9 \pm 1.4) \times 10^{-3}$). We see the difference between adventitious carbon and fabrication residue starkly when we compare the untreated aluminum device loss tangent with the 49% HF treated aluminum loss tangent that was left to saturate in both hydrocarbons and oxide over 90 days. The 49% HF acid-treated device after exposure to atmosphere for 90 days shows a C1s intensity $\sim 8\%$ less than the signal observed for untreated devices (Fig. 4e). However, the sources of hydrocarbon contamination are different in each case: the untreated devices are mainly contaminated by fabrication hydrocarbon residue, and the 49% HF acid-treated device after exposure to atmosphere for 90 days contains only adventitious hydrocarbons. Despite a similar hydrocarbon coverage estimated by XPS, the surface loss tangent for the device treated with 49% HF and left in atmosphere for 90 days has 21% less TLS loss despite having 15% more oxide. Comparing these surface loss tangents suggests that the loss contribution from the adventitious hydrocarbons must be much lower than that of fabrication residue, and is therefore negligible compared to the TLS losses for aluminum oxide, fabrication residue, and the SA and MS interfaces.

We combine the measured losses at each interface to estimate a loss budget for aluminum resonators. For a co-planar waveguide resonator with a $10 \mu\text{m}$ gap fabricated from aluminum with no further surface processing, we estimate aluminum oxide to account for $(52.4 \pm 21.5)\%$, hydrocarbons for $(27.7 \pm 7.2)\%$, and the MS and SA surfaces combined for $(19.8 \pm 15.9)\%$ of surface TLS losses. Furthermore, we can estimate the contribution of surface TLS loss in the aluminum Josephson junction leads to the total loss in state-of-the-art Ta-on-Si transmon qubits [1]. We simulate the electric field energy density of the resonant qubit mode while ignoring a small radius around the junction barrier oxide because of the difficulty of obtaining accurate electric field simulations at the tunnel barrier. We then use the measured loss tangents at a microwave power that corresponds to one intracavity photon ($\bar{n} = 1$), the relevant parameter range for qubit operation, to compute the contribution of each interface to the total qubit relaxation rate. We note that at $\bar{n} = 1$, the surface loss tangent for AlO_x , $\tan \delta_{\text{AlO}_x, \bar{n}=1}$, is reduced by a factor of five compared to linear absorption ($\bar{n} = 0$) (Online Resource S7). We

find that 19.7% of the TLS loss in state-of-the-art transmon qubits with the geometry reported in [1] arises from the surfaces of the Al leads associated with the Josephson junction, while 73.5% is attributed to the Ta-based capacitor pads. We then compare the simulated qubit shunt capacitance with the calculated parallel-plate capacitance of the junction and solve for the remaining TLS loss arising from the junction barrier itself, and attribute 6.8% of the total TLS loss to the barrier of the Josephson junction. Notably, the aluminum leads have an effective Q of 48 million, thereby representing an important target for loss mitigation.

Comparing these loss estimates to the performance of Ta-on-Si qubits, we estimate that the tunnel barrier itself must have a Q greater than 142 million, which implies that the loss tangent of the aluminum oxide junction barrier, $\tan \delta_{\text{AlO}_x, \text{barrier}, \bar{n}=1} = (4.3 \pm 3.7) \times 10^{-7}$, is four orders of magnitude lower than the surface oxide $\tan \delta_{\text{AlO}_x, \bar{n}=1}$. This low tunnel barrier loss tangent estimate is consistent with previous estimates of the tunnel barrier loss tangent in “mergemon” geometries [36]. A likely source for this discrepancy is a low spectral and areal density of TLSs leading to the complete absence of strongly-coupled TLSs in the junction. In the geometry used in Ref. [1], the junction has dimensions $A_{\text{JJ,dielectric}} = 200 \text{ nm} \times 200 \text{ nm} = 4 \times 10^{-2} \mu\text{m}^2$, $V_{\text{JJ,dielectric}} = A_{\text{JJ,dielectric}} \times 2 \text{ nm} = 8 \times 10^{-5} \mu\text{m}^3$. In junctions with comparable area, values of ~ 0.5 -1.5 TLS (GHz μm^2) $^{-1}$ and 250-760 TLS (GHz μm^3) $^{-1}$ have previously been reported [28, 37–40]. This corresponds to a predicted 0.02 to 0.06 TLS per GHz for a 200 nm by 200 nm area (200 nm by 200 nm by 2 nm volume) junction. The low observed loss tangent also implies that the primary source of microwave loss is TLSs. Therefore avoiding strongly coupled TLS is sufficient to achieve a low-loss junction tunnel barrier in individual qubits, though improvements in TLS density will be needed to ensure consistent performance across all qubits in large-scale processors.

We lastly compare the TLS loss in Al resonators to Ta resonators. Ta is chemically robust, a property that allows for more aggressive post-fabrication processes such as piranha solution (2:1 H_2SO_4 : H_2O_2) and buffered oxide etch (BOE), which reduces surface oxides with slow oxide regrowth kinetics and eliminates the fabrication hydrocarbon contamination. These properties enable state-of-the-art tantalum resonators with loss tangents of $(1.59 \pm 0.07) \times 10^{-3}$ (Fig. 3b, black data) and $(8.1 \pm 0.6) \times 10^{-4}$ (Fig. 3b, gray data), respectively [2]. The 49% HF acid-treated Al resonators perform within 1σ of the piranha-treated Ta devices; however, BOE-treated Ta devices show two times lower TLS loss than HF-treated Al devices. To achieve comparable surface losses to BOE-treated Ta, the aluminum oxide thickness would need to be decreased to about 0.5 nm, which is incompatible with procedures for standard packaging and wiring in ambient conditions because of aluminum’s fast oxide growth kinetics.

IV. CONCLUSION

In this study, we use microwave measurements of Al resonators and correlate them with detailed materials characterization to quantify loss mechanisms. We find that the dominant

source of loss is TLSs associated with the surface aluminum oxide, which is four times more lossy than the surface oxide of Ta in state-of-the-art devices. This loss can be mitigated by treatment with 49% HF, which reduces the oxide thickness by ~ 0.8 nm and thereby reduces the surface losses by a factor of 1.8; however, rapid surface oxide regrowth makes this surface condition difficult to translate to large-scale processors. Our results also suggest that differences in film crystallinity and morphology have a small contribution to the total surface loss compared to aluminum oxide and hydrocarbon contamination related to fabrication residue. Our measurements of aluminum and aluminum oxide allow us to estimate that they contribute around 27% of the relaxation rate of state-of-the-art Ta qubits [1] (Online Resources S7 and S8). These results underscore the importance of surface cleaning and surface oxide mitigation in continued improvement of transmon qubits. Ongoing work targets the suppression of surface oxide regrowth in Al devices via full encapsulation and the optimization of post-fabrication cleaning to mitigate fabrication residues and surface oxides near the Josephson junctions of Ta qubits. Furthermore, the TLS loss associated with the surface of Al is a potential source of temporal fluctuations and dephasing from strongly-coupled TLSs [28, 40, 41], and eliminating these TLSs will be important for improving the performance of large-scale superconducting quantum processors.

V. MATERIALS AND METHODS

A. Film growth

Prior to film deposition of heated films, we clean 1” by 1” pieces of c-plane HEMEX grade sapphire substrates (Crystal Systems) in a 2:1 H_2SO_4 : H_2O_2 piranha solution to rid the substrate surface of hydrocarbon residue. We rinse the substrates in DI water three times, submerged in IPA and blow dried with a nitrogen gun. We load the sapphire into the loadlock of an e-beam evaporator (Plassys MEB550S) and transfer to the deposition chamber after reaching a vacuum of 5×10^{-7} mTorr in the loadlock. We heat the sapphire to 300°C in situ for one hour, then cool to 200°C for deposition. We deposit aluminum films from an unlined copper crucible at a rate of 0.25 nm/s and a thickness of 200 ± 10 nm as measured by a quartz crystal monitor at a base pressure of 2.9×10^{-10} mTorr. After deposition, we let films cool to ambient temperature in vacuum over the course of 12 hours.

For cryogenically deposited films, the substrate with patterned resist is loaded into the loadlock, transferred to the deposition stage and cooled using a liquid N_2 cold finger which directly contacts the substrate holder. When a steady state temperature is reached (-72°C), the cold finger is retracted and aluminum is deposited using the same specifications as above. Films are left to warm in vacuum to ambient temperature over the course of 12 hours.

For the aluminum film deposited at room temperature on high-resistivity silicon ($> 20 \text{ k}\Omega \text{ cm}$, Siebert), we use piranha solution (same as above) to remove hydrocarbons and oxidize the surface. Next, we submerge the silicon substrate in a 10:1 DI water:HF solution for 3 minutes to remove the surface oxide. After rinsing 3 times with DI water and drying completely with

nitrogen, we transfer silicon to the Plassys loadlock within 10 minutes to ensure no interfacial oxide [1]. We evaporate the Al film at a rate of 0.4 nm/s and transfer the substrate out immediately after finishing.

B. Device fabrication

For devices with subtractive etching (wet etching or reactive ion etching), we grow aluminum films prior to fabrication. We prepare the surface with hexamethyldisilazane (HMDS) at 148°C in a YES vapor prime oven to promote adhesion of the resist onto the surface. We spin AZ1518 onto the film at 4000 rpm for 40 seconds then bake at 95°C for one minute on a hotplate. We then use direct-write lithography (Heidelberg DWL66+) to define the resonator pattern using the 10mm writehead. We hard bake the resist on a hot plate at 110°C for two minutes, then develop using AZ300MIF developer for 90 seconds, followed by a 30s rinse in deionized (DI) water and drying using a nitrogen gun.

We use both wet etching and reactive ion etching (RIE) to define device features. For wet etched devices, we place samples in a mixture of 55-65% phosphoric acid, 1-5% nitric acid, 5-10% acetic acid and balanced DI water (Transene Aluminum Etchant Type A) for 7-10 minutes at room temperature, removing the film roughly one minute after the features become visible. We rinse the device in DI water three times and blow dry with a nitrogen gun. For dry etch devices, we use a chlorine-based chemistry in an inductively coupled plasma reactive ion etcher (PlasmaTherm Takachi SLM) with a pressure of 4 mTorr, flow rate of 1.5 sccm Cl₂, 3 sccm BCl₃, and 25 sccm Ar, bias power of 70W, RF power of 300W at 25°C for 75s.

For samples fabricated using liftoff, we employ the same HMDS prime directly on the sapphire substrate. We spin a bilayer resist stack of LOR 3A and AZ1518 to achieve a small undercut to ensure clean liftoff. We spin LOR 3A at 4000 rpm for 40s and bake for 5 minutes at 160°C, followed by AZ1518, spun and baked with the above parameters. Photolithography follows the same procedure as above, but the AZ300MIF development is 2 minutes long to achieve an undercut in the bilayer. After rinsing in DI water and drying using a N₂ gun, we finish with a five minute, 500W O₂ ashing step (Tepla IoN O₂ Etcher) to clean the substrate and improve adhesion of the metal layer.

For all samples, we remove resist using Remover PG at 80°C for two hours, followed by sonication in acetone and IPA for 5 minutes and drying using a nitrogen gun. We then clean devices using a solvent series, 30% H₂O₂, or 49% HF, and subsequently wirebond and package (QDevil QCage.24).

C. Surface cleaning

Three different cleanings were used to study surface losses on aluminum devices: a solvent series, 30% H₂O₂ or 49% HF. The solvent series was designed to minimize hydrocarbon residue while not damaging the underlying aluminum and consisted of two cycles of various polar aprotic, polar protic and nonpolar solvents, where each solvent is miscible with the previous one. The exact cycle is as follows, where the device

is sonicated in each solvent for 20 minutes unless specified: DI water, acetone, pentane, methanol, acetone, toluene, acetone (5 min), IPA (5 min). The chip is finally nitrogen dried and packaged immediately.

30% H₂O₂ was utilized to more aggressively target hydrocarbons after the solvent series showed noticeable carbon contamination in XPS. Devices were placed into roughly 30 mL of 30% H₂O₂ and left for 30 minutes. After H₂O₂, the device was rinsed three times in DI water, sonicated in IPA for 5 minutes and blow dried with nitrogen.

49% HF was utilized to fully remove the surface oxide and any associated surface contaminants. The device was submerged in 49% HF for 5-20 seconds and then quickly rinsed into successive DI water 5 times, then sonicated for 5 minutes in IPA and blow dried with nitrogen. After HF treatment on sapphire substrates, we observed variability in the uniformity of aluminum oxide etching, which we attributed to non-uniformity of the starting aluminum film surface, such as an unsaturated oxide or micro-masking from hydrocarbon residue that was still present on the device. Because this treatment is only 5-10s, small changes in the surface chemistry such as these can lead to visible variations in the aluminum surface after the treatment. After seeing this issue, we took steps to saturate the oxide and remove hydrocarbons prior to the HF treatment by implementing a five minute, 500W O₂ ashing step (Tepla IoN O₂ Etcher) before submerging Al on Si devices in HF, as we iterated on sapphire to first test the feasibility of the HF treatment before attempting to do so on silicon. We verified in XPS that all residual fabrication hydrocarbons were removed and that the oxide was slightly grown.

VI. ACKNOWLEDGMENTS

We acknowledge Lev Krayzman, Sounak Mukherjee, ad Bert Harrop for helpful discussions. This work was primarily supported by the U.S. Department of Energy, Office of Science, National Quantum Information Science Research Centers, Co-design Center for Quantum Advantage (C²QA) under Contract No. DESC0012704. This material is based upon work supported by Google Quantum AI under SOW No. 89201. This material is based upon work supported by the Air Force Office of Scientific Research under award number FA9550-25-1-0172. E. H. and M. P. B. were also supported by the National Science Foundation Graduate Research Fellowship Program (NSF GRFP) under grant No. DGE-2444107. The authors acknowledge the use of Princeton’s Imaging and Analysis Center (IAC), which is partially supported by the Princeton Center for Complex Materials (PCCM), a National Science Foundation (NSF) Materials Research Science and Engineering Center (MRSEC; DMR-2011750), as well as the Princeton Micro/Nano Fabrication Laboratory.

Princeton University Professor Nathalie de Leon is a Visiting Faculty Researcher with Google Quantum AI. Due to her income from Google, Princeton University has a management plan in place to mitigate a potential conflict of interest that could affect the design, conduct, and reporting of this research. Her academic group also has a sponsored research contract with Google Quantum AI. Princeton University Professor Andrew Houck is also a consultant for Quantum Circuits Incorporated

(QCI). Due to his income from QCI, Princeton University has a management plan in place to mitigate a potential conflict of

interest that could affect the design, conduct, and reporting of this research.

-
- [1] M. P. Bland, F. Bahrami, J. G. C. Martinez, et al. 2d transmons with lifetimes and coherence times exceeding 1 millisecond. *Nature*, 647(1):343–348, 2025.
- [2] K.D. Crowley, R. A. McLellan, A. Dutta, et al. Disentangling losses in tantalum superconducting circuits. *Phys. Rev. X*, 13(4):041005, 2023.
- [3] Y. Zhao, Y. Ye, H.-L. Huang, et al. Realization of an error-correcting surface code with superconducting qubits. *Phys. Rev. Lett.*, 129(3):030501, 2022.
- [4] Google Quantum AI. Suppressing quantum errors by scaling a surface code logical qubit. *Nature*, 614(7949):676–681, 2023.
- [5] Google Quantum AI and Collaborators. Quantum error correction below the surface code threshold. *Nature*, 638(8052):920–926, 2025.
- [6] N. Lacroix, A. Bourassa, F. J.H. Heras, et al. Scaling and logic in the color code on a superconducting quantum processor. *Nature*, pages 1–3, 2025.
- [7] N. Ofek, A. Petrenko, R. Heeres, et al. Extending the lifetime of a quantum bit with error correction in superconducting circuits. *Nature*, 536(7617):441–445, 2016.
- [8] V. V. Sivak, A. Eickbusch, B. Royer, et al. Real-time quantum error correction beyond break-even. *Nature*, 616(7955):50–55, 2023.
- [9] S. Ganjam, Y. Wang, Y. Lu, et al. Surpassing millisecond coherence in on chip superconducting quantum memories by optimizing materials and circuit design. *Nat. Commun.*, 15(1):3687, 2024.
- [10] L. Krayzman, C. U. Lei, S. Ganjam, et al. Superconducting quantum memory with a suspended coaxial resonator. *App. Phys. Lett.*, 124(20), 2024.
- [11] A. R. Matanin, K. I. Gerasimov, E. S. Moiseev, et al. Toward highly efficient multimode superconducting quantum memory. *Phys. Rev. Appl.*, 19(3):034011, 2023.
- [12] R. Barends, L. Lamata, J. Kelly, et al. Digital quantum simulation of fermionic models with a superconducting circuit. *Nat. Commun.*, 6(1):7654, 2015.
- [13] S. Kumar, N. N. Hegade, A.-M. Visuri, et al. Digital-analog quantum computing of fermion-boson models in superconducting circuits. *npj Quantum Inf.*, 11(1):43, 2025.
- [14] D. Marcos, P. Rabl, E. Rico, and P. Zoller. Superconducting circuits for quantum simulation of dynamical gauge fields. *Phys. Rev. Lett.*, 111(11):110504, 2013.
- [15] A. Kandala, A. Mezzacapo, K. Temme, et al. Hardware-efficient variational quantum eigensolver for small molecules and quantum magnets. *Nature*, 549(7671):242–246, 2017.
- [16] J. Biznárová, A. Osman, E. Rehnman, et al. Mitigation of interfacial dielectric loss in aluminum-on-silicon superconducting qubits. *npj Quantum Inf.*, 10(1):78, 2024.
- [17] R. D. Chang, N. Shumiya, R. A. McLellan, et al. Eliminating surface oxides of superconducting circuits with noble metal encapsulation. *Phys. Rev. Lett.*, 134(9):097001, 2025.
- [18] J. Verjauw, R. Acharya, J. Van Damme, et al. Path toward manufacturable superconducting qubits with relaxation times exceeding 0.1 ms. *npj Quantum Inf.*, 8(1):93, 2022.
- [19] M. Zemlicka, E. Redchenko, M. Peruzzo, et al. Compact vacuum-gap transmon qubits: Selective and sensitive probes for superconductor surface losses. *Phys. Rev. Appl.*, 20(4):044054, 2023.
- [20] Z.-H. Zhang, K. Godeneli, J. He, et al. Acceptor-induced bulk dielectric loss in superconducting circuits on silicon. *Phys. Rev. X*, 14:041022, 2024.
- [21] A. P. M. Place, L.V.H Rodgers, P. Mundada, et al. New material platform for superconducting transmon qubits with coherence times exceeding 0.3 milliseconds. *Nat. Commun.*, 12(1):1779, 2021.
- [22] C. Wang, X. Li, H. Xu, et al. Towards practical quantum computers: Transmon qubit with a lifetime approaching 0.5 milliseconds. *npj Quantum Inf.*, 8(1):3, 2022.
- [23] Nathalie de Leon. How to build a long-lived qubit. *Nat. Phys.*, 21(1):1500–1503, 2025.
- [24] L. Zeng, D. T. Tran, C.-W. Tai, et al. Atomic structure and oxygen deficiency of the ultrathin aluminium oxide barrier in Al/AlOx/Al Josephson junctions. *Sci. Rep.*, 6(1):29679, 2016.
- [25] S. Fritz, L. Radtke, R. Schneider, et al. Structural and nanochemical properties of AlOx layers in Al/AlOx/Al-layer systems for Josephson junctions. *Phys. Rev. Mat.*, 3(11):114805, 2019.
- [26] T. C. DuBois, M. C. Per, S. P. Russo, and J. H. Cole. Delocalized oxygen as the origin of two-level defects in Josephson junctions. *Phys. Rev. Lett.*, 110(7):077002, 2013.
- [27] J. Lisenfeld, G. J. Grabovskij, C. Müller, et al. Observation of directly interacting coherent two-level systems in an amorphous material. *Nat. Commun.*, 6(1):6182, 2015.
- [28] J. Lisenfeld, A. Bilmes, A. Megrant, et al. Electric field spectroscopy of material defects in transmon qubits. *npj Quantum Inf.*, 5(1):105, 2019.
- [29] C. Kittel. *Introduction to Solid State Physics*. Wiley, New York, 2004.
- [30] N. Cabrera and N. F. Mott. Theory of the oxidation of metals. *Rep. Prog. Phys.*, 12(1):163, 1949.
- [31] L. P. Ramírez, F. Bournel, J.-J. Gallet, et al. Testing the Cabrera–Mott oxidation model for aluminum under realistic conditions with near-ambient pressure photoemission. *J. Phys. Chem. C.*, 126(1):2517–2530, 2022.
- [32] N. Cai and G. Zhou. Tuning the limiting thickness of a thin oxide layer on Al(111) with oxygen gas pressure. *Phys. Rev. Lett.*, 107(1):035502, 2011.
- [33] J. D. Baran, H. Grönbeck, and A. Hellman. Mechanism for limiting thickness of thin oxide films on aluminum. *Phys. Rev. Lett.*, 112(1):146103, 2014.
- [34] C. M. Lousada and P. A. Korzhavyiab. The first stages of oxide growth at the low index Al surfaces (100), (110), (111): clusters and stripes vs. homogeneous growth. *Phys. Chem. Chem. Phys.*, 20(1):29549–29557, 2018.
- [35] C. Lanthony, J. M. Ducéré, M. Djafari Rouhani, et al. On the early stage of aluminum oxidation: An extraction mechanism via oxygen cooperation. *J. Chem. Phys.*, 137(1):094707, 2012.
- [36] H.J. Mamin, E. Huang, S. Carnevale, et al. Merged-element transmons: Design and qubit performance. *Phys. Rev. Appl.*, 16:024023, Aug 2021.
- [37] A. Osman, J. Fernández-Pendás, C. Warren, et al. Mitigation of frequency collisions in superconducting quantum processors. *Phys. Rev. Res.*, 5:043001, Oct 2023.
- [38] J. M. Martinis, K. B. Cooper, R. McDermott, et al. Decoherence in Josephson qubits from dielectric loss. *Phys. Rev. Lett.*, 95:210503, Nov 2005.
- [39] J. S. Kline, H. Wang, S. Oh, et al. Josephson phase qubit circuit for the evaluation of advanced tunnel barrier materials. *Supercond. Sci. Technol.*, 22:015004, Nov 2008.

- [40] A. Bilmes, S. Volosheniuk, A. V. Ustinov, and J. Lisenfeld. Probing defect densities at the edges and inside Josephson junctions of superconducting qubits. *npj Quantum Inf.*, 8(1):24, 2022.
- [41] D. Colao Zanuz, Q. Ficheux, L. Michaud, et al. Mitigating losses of superconducting qubits strongly coupled to defect modes. *Phys. Rev. Appl.*, 23:044054, Apr 2025.